Article

Hierarchically, Low Band Gap Nanohybrid InVO$_4$-CdS Heterojunction for Visible Light-Driven Toxic Organic Dye Degradations

Balachandran Subramanian,* Zhongshan Xu, Kumaravel Jeeva Jothi, Emad Makki, Selvamani Muthamizh, Dhilip Kumar Rajaiah, Natarajan Prakash, Nagarani Sandran, Jayant Giri,* Feng Wang,* and Mingshu Yang*

Read Online

ACCESS | Metrics & More | Article Recommendations | SI Supporting Information

ABSTRACT: The synthesis of InVO$_4$-CdS heterojunction photocatalysts has been achieved by a novel two-step approach, including a microwave-assisted technique, followed by a moderate hydrothermal method, marking the first successful instance of such a synthesis. X-ray diffraction, field-emission scanning electron microscopy, elemental color mapping, high-resolution transmission electron microscopy, UV− vis diffuse reflectance spectroscopy, Raman analysis, photoluminescence, X-ray photoelectron spectroscopy, and Brunauer−Emmett−Teller were employed to investigate the crystal structures, surface morphologies and particle sizes, chemical compositions, and optical characteristics of the as-synthesized materials. The research results indicated that the heterojunction InVO$_4$-CdS, as synthesized, consisted of InVO$_4$ microrods with an average size of around 15 nm and cadmium sulfide (CdS) microflowers with a diameter of 1.5 μm. Furthermore, all of the heterojunctions had favorable photoabsorption properties throughout the visible-light spectrum. The photocatalytic efficiency of the samples obtained was thoroughly assessed by the degradation of acid violet 7 (AV 7) under visible light irradiation with a wavelength greater than 420 nm. The photocatalytic efficiency for the decomposition of AV 7 was greatly enhanced in the InVO$_4$-CdS (IVCS) heterojunctions when compared to prepared bare InVO$_4$ and CdS. Additionally, it was observed that the composite material consisting of IVCS 3 wt % InVO$_4$ combined with CdS exhibited the most significant enhancement in catalytic effectiveness for the photodegradation of AV 7 dye. Specifically, the catalytic performance of this composite material was found to be around 69.4 and 76.2 times greater than that of pure InVO$_4$ and CdS, respectively. Furthermore, the experimental procedure including active species trapping provided evidence that h$^+$ and •O$_2^-$ radicals were the primary active species involved in the photocatalytic reaction process. Additionally, a potential explanation for the improved photocatalytic activity of the InVO$_4$-CdS heterojunction was presented, taking into account the determination of band positions.
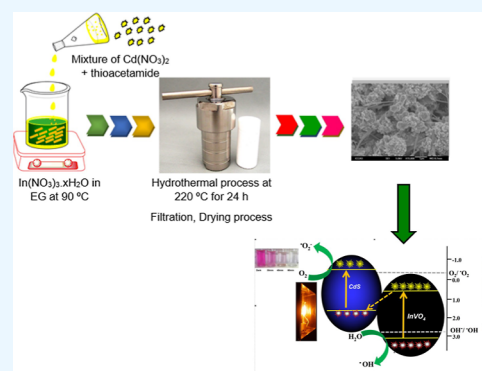
1. INTRODUCTION

A long-term and sustainable energy supply is guaranteed by the natural replenishment of green energy resources, including sunshine, wind, and water. They do not consume limited resources as fossil fuels do, preserving important reserves for future generations. In comparison to fossil fuels, the renewable energy industry often creates more employment per unit of energy generated, boosting local economies. Although using green energy has many benefits, it is crucial to recognize that there are still some drawbacks, including the intermittent nature of certain renewable energy sources, such as solar and wind, the limits of energy storage, and the high initial prices. However, ongoing research and development is addressing these issues, making green energy a more sensible and alluring option for a sustainable future.[1]

In the past few years, there has been remarkable research and growth in the area of semiconductor photocatalysis, and huge numbers of researchers have concentrated on exploiting novel and highly efficient visible-light-active photocatalysts for the degradation of toxic organic pollutants. Photocatalysis using semiconductor nanomaterials has earned increasing attention for resolving worldwide pollution problems. The major uses of this skill are the degradation of harmful organic dyes, and toxic materials have attracted a lot of attention in water treatment.[2] During the natural sun- or visible-light-induced method, the engendered electron/hole (e$^-$ and h$^+$ pair) must transfer to the surface of material-active reaction sites to reduce protons and oxidize water molecules. The efforts have also motivated environmental remediation as industrial toxic wastes often contain a major amount of synthetic organic dyes.[3]
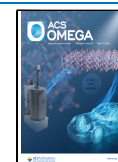
Indium vanadate ($InVO_4$) has been established to be a fascinating, more important visible light-active semiconductor nanomaterial. $InVO_4$ has generally been used as anode materials for lithium-ion batteries, promising fundamental photocatalysts[4−6] and electrochemical detection[7] due to its narrow band gap (approximately 2.0 eV) and distinctive optical and electrical behavior being capable of absorbing extra visible light and chemical stability.[8,9] $InVO_4$ has two highly stable crystal phase assemblies, monoclinic and orthorhombic.[10,11] Among the two phases, orthorhombic $InVO_4$ has been comprehensively used in wastewater treatment, like the degradation of toxic pollutants and water splitting under visible light.[12] Indium orthovanadate ($InVO_4$) has garnered significant attention in the field of photocatalysis due to its potential use in many applications, including pollution abatement and solar energy harvesting. The band gap of $InVO_4$ lies in the range of the electromagnetic spectrum where visible light exists. As a result, it is suited for photocatalytic applications in solar lighting since it can absorb a significant amount of sunlight. When exposed to light, $InVO_4$'s photocatalytic activity kicks into its maximum level, accelerating and facilitating chemical processes. Absorbing light causes it to produce electron−hole pairs, which may then take part in redox processes, such as the destruction of contaminants or the transformation of molecules. Successful photocatalysis relies on efficient charge separation. Due to its unique crystal structure and electrical characteristics, $InVO_4$ may aid in the separation of photogenerated electron−hole pairs. Indium, vanadium, and oxygen are the generally nontoxic components that make up $InVO_4$.[12] In comparison to other photocatalytic compounds based on rare or precious metals, these elements are both more widely available and less costly. Under the right circumstances, $InVO_4$ may show high stability, which extends the time period during which its photocatalytic activity can function. When the photocatalyst's effectiveness is required over long periods, its stability is essential. In addition, several reports specify that the preferred surface morphology and size of nanomaterials could control the position of the energy band (conduction and valence bands) for greater redox ability.[13,14] However, indium vanadate has a great electron (e^-) and hole (h^+) pair recombination rate, and it reduces the efficiency of the photocatalytic activity of semiconductor materials. To succeed in a great photocatalytic activity, $InVO_4$ has been modified by different approaches such as highly active metal ion doping[15,16] and the formation of semiconductor couple oxide composites.[17−20] To encounter forthcoming environmentally friendly requirements, it is still desirable to improve several new visible light-active photocatalyst materials to further increase photocatalytic efficacy.[21,22]

Cadmium sulfide (CdS) is a semiconductor that has gained significant attention in scientific studies due to its narrow band gap of 2.4 eV and its ability to act as a visible light-driven photocatalyst. The material is particularly noteworthy as it belongs to the II−VI group of semiconductors and possesses a direct bulk-phase band gap that aligns closely with the electromagnetic spectrum of solar radiation. Additionally, CdS is highly regarded for its cost-effectiveness, further contributing to its widespread study and exploration. The investigation of CdS has been extensively conducted by the technique of doping with foreign elements as well as the formation of solid solutions or composites with other semiconductors. CdS-based photocatalytic devices may be cost-effective since cadmium is widely available and affordable.

Photons (light particles) are converted into usable energy when they strike CdS nanoparticles. Electrons are boosted from the valence band (VB) to the conduction band (CB) as an outcome of this absorption, forming electron−hole pairs. In the VB, a positively charged hole is left behind when an electron is promoted to the CB. In photocatalysis, electron−hole pairs are the principal active species. Water and carbon dioxide molecules, for example, may be reduced by CB electrons to produce hydrogen gas and hydrocarbon compounds. The oxidation of organic contaminants and other molecules via VB holes may reduce their toxicity.

Researchers have recently created heterojunction photocatalytic systems made of $InVO_4$ to make the process of breaking down toxic organic pollutants more effective. In their study, Ji et al.[23] made $InVO_4/BiVO_4$ photocatalysts that made visible light better at breaking down RhB and MB dye molecules. For enhanced visible-light photocatalytic performance in RhB degradation, Shi et al. achieved $InVO_4/g\text{-}C_3N_4$ heterojunctions.[24,25] Researchers mostly fabricated $InVO_4$ heterojunction photocatalysts using hydrothermal synthesis. However, the large size (micron range) of the materials made from them meant they had a small surface area and poor photocatalytic abilities. Assembly of heterostructures was formed by coupling one or more energetic components, such as $InVO_4/CdS$,[8] NiS/CdS,[26] $TiO_2/InVO_4/RGO$,[19] MoS_2/CdS,[27] $C_3N_4−CdS$,[28] $Pt−PdS/CdS$,[29] CdS-MCM 48,[30] $Zn_{1−x}Cd_xS$,[31,32] $CdIn_2S_4$,[33] $BiOBr−CdS$,[34] Fe_3O_4/CdS,[35] $Co_3O_4−CdS$,[36] $CdS/ZnS/In_2S_3$,[37] and CdS/TiO_2.[38] This kind of coupled semiconductor nanomaterials, the heterojunction interface formed between the semiconductors of identical VB and CB potentials, is created. In this manner, the electric field-supported charge conveyance from one semiconductor to the other via interfaces is encouraging for the electron−hole separation in the coupled semiconductor nanomaterials and the resultant electron (e^-) or hole (h^+) richness on the surfaces of the two semiconductors.[39−42]

In this work, we report a novel ternary heterostructured $InVO_4$-CdS that has been synthesized by the hydrothermal method. The obtained $InVO_4$-CdS composites significantly enhanced the photocatalytic activity in the degradation of Acid violet 7 (AV 7) in aqueous solution under visible light irradiation at neutral pH and relatively high-stability, activities than $InVO_4$ and CdS. The results prove that the heterojunction interface formation of CdS and $InVO_4$ is significantly improved in the existence of CdS under visible light. CdS particles are exceedingly small and can perform an outstanding coverage on larger crystals, hence it is easy to form core−satellite heterojunction nanomaterials to conveyance photogenerated carriers (e^- and h^+) through the interaction among CdS and $InVO_4$.

2. EXPERIMENTAL METHODS

2.1. Materials and Methods. All of the chemicals employed in the fabrication of nanomaterials and analysis were of analytical reagent quality and therefore required no additional purification before use. $InCl_3 \cdot 4H_2O$, $Cd(NO_3)_2 \cdot 4H_2O$, ammonium metavanadate (NH_4VO_3, Sigma-Aldrich, US, 99.6%), ammonium hydroxide (NH_4OH, Sigma-Aldrich, US, 30%), nitric acid (HNO_3, Merck, Germany, 65%), and thioacetamide (TAA) were used. Deionized water was used throughout the preparation and analysis.

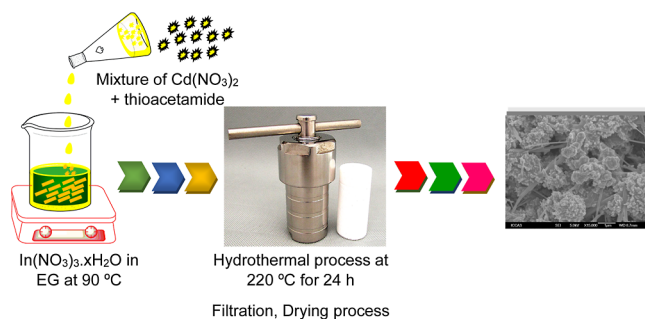**2.2. $InVO_4$ Preparation.** The hydrothermal—thermal decomposition process was used for the preparation of

$InVO_4$. In a distinctive procedure, we used $InCl_3 \cdot 4H_2O$ (2 mmol) dissolved in 50 mL of deionized water (sol 1). At the same time, NH_4VO_3 solid (2 mmol) was dissolved in 47 mL of deionized water and 3 mL of HNO_3 acid (sol 2), followed by vigorous stirring for 3 h to obtain a clear solution and added to the above-mentioned solution to obtain a yellowish solution. The solutions were added dropwise to form a yellow color solution and soon subsequently stirred for a further 3 h at room temperature. Then, 6.0 M NH_4OH was gradually added to the above solutions to adjust the pH to 8. Subsequently, the mixture was introduced into a Teflon-lined stainless-steel autoclave with a volume of 100 mL and subjected to hydrothermal treatment at a temperature of 220 °C for a duration of 24 h. After the reactor was cooled to ambient temperature, the resultant materials underwent centrifugation. Afterward, the samples underwent a triple washing process using deionized water, ethanol, and acetone. Subsequently, they were air-dried at a temperature of 80 °C and subsequently subjected to heat treatment at 500 °C for 6 h.

2.3. CdS Preparation. A transparent solution of the cadmium precursor (cadmium nitrate) was used in deionized water. CdS microflowers may be made smaller or larger, depending on the concentration. TAA could be used as a sulfur precursor if it is dissolved in deionized water. According to the intended stoichiometry of CdS, the Cd/S molar ratio must be maintained. A glass beaker was prepared with the cadmium precursor solution. Drop by drop, continuously stirring, the sulfur precursor mixture was added to the cadmium precursor solution. While stirring, ammonium hydroxide (NH_4OH) was added to raise or lower the solution's pH. A pH of 10 to 11 was ensured. The mixture was then loaded into a 100 mL Teflon-lined stainless-steel autoclave treated at a temperature of 220 °C for 24 h. This procedure aids in the regulation of the onset and development of CdS crystals. The reaction mixture was kept stirred while it heated up. The solution is typically heated to a temperature of 80 °C. Taking this action encourages the formation of CdS crystals.

2.4. $InVO_4$-CdS Preparation. The $InVO_4$-CdS heterostructures were synthesized by using an efficient hydrothermal technique, as shown in Scheme 1. In the experimental

Scheme 1. Preparation of $InVO_4$-CdS Heterostructures

Mixture of $Cd(NO_3)_2$ + thioacetamide

$In(NO_3)_3 \cdot xH_2O$ in EG at 90 °C

Hydrothermal process at 220 °C for 24 h

Filtration, Drying process

procedure, a suspension was created by dispersing 1 mmol $Cd(NO_3)_2 \cdot 4H_2O$ and varying amounts of as-made $InVO_4$ were added to 50 mL of deionized water. The dispersion process included magnetic stirring for 30 min. Next, a solution containing 2 mmol H_2NCSNH_2 was dissolved in 10 mL of deionized water. This solution was then gradually introduced into the previously described suspension, allowing for an additional 30 min of reaction time. As a result, a combination

was obtained. Subsequently, the mixture was carefully transferred into a Teflon-lined autoclave with a capacity of 100 mL. The autoclave was then subjected to heating at a temperature of 220 °C for 24 h. Following the completion of the heating process, the autoclave was allowed to cool down to room temperature naturally. The resulting products were subsequently subjected to centrifugation and washed three times with deionized water and ethanol. Finally, the products were dried in ambient air at a temperature of 80 °C for 12 h. To enhance clarity, the composites of $InVO_4$-CdS with anticipated $InVO_4$ concentrations of 0, 1, 2, 3, and 5 wt % are denoted as pure CdS, IVCS-1, IVCS-2, IVCS-3, and IVCS-5, correspondingly.

3. RESULTS AND DISCUSSION

X-ray diffraction (XRD) analysis was carried out to ascertain the composition, crystal structure, and orientation of the prepared catalyst materials. Figure 1A shows the XRD patterns of the different samples such as (a) CdS, (b) $InVO_4$, and (c) $InVO_4$-CdS, respectively. The peaks at 2θ values of 24.9, 26.52, 28.23, 36.56, 43.74, 47.91, and 51.93° were assigned to
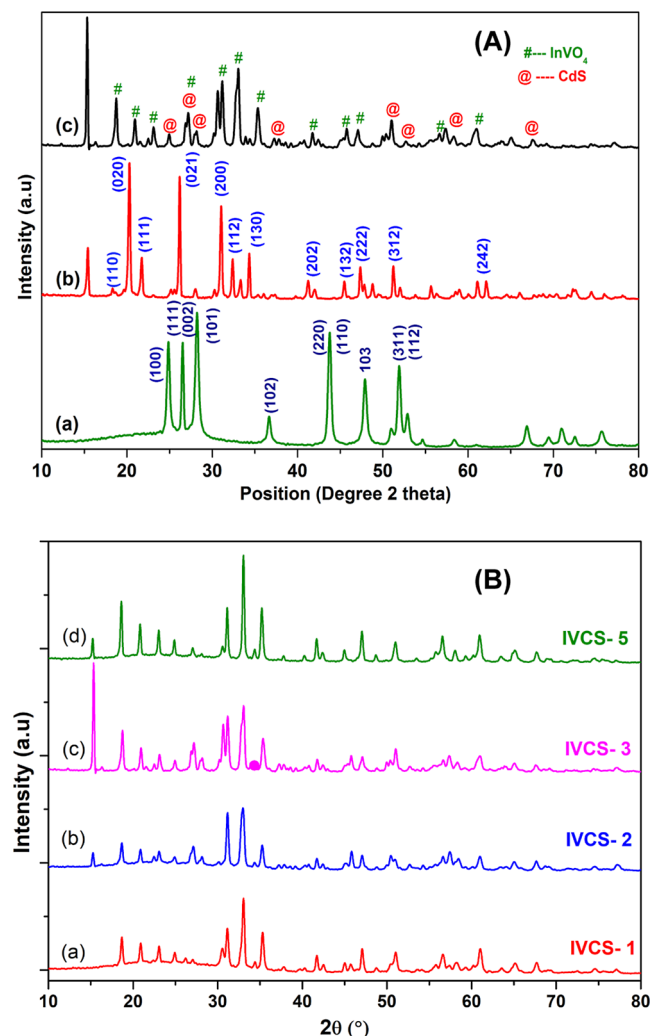

Figure 1. (A) Powder XRD patterns of (a) prepared CdS, (b) prepared $InVO_4$, and (c) IVCS-3. (B) Powder XRD patterns of various concentrations of InVO−CdS: (a) IVCD-1, (b) IVCD-2, (c) IVCD-3, and (d) IVCS-5.

diffraction patterns from the (100), (002), (101), (102), (110), (103), and (112) crystal planes of CdS (JCPDS#41-1049), respectively, demonstrating that the highly crystallized CdS was effectively synthesized [Figure 1A(a)]. In the same way, the strong peaks appearing at around 24.8, 28.3, 36.8, and 47.8° are due to hexagonal CdS. The diffraction peaks displayed $InVO_4$ at 2θ of 18.3, 20.41, 21.77, 26.03, 28.10, 30.96, 32.31, 34.37, 41.23, 47.32, 55.53, and 62.24° can be indexed to the (110), (020), (111), (021), (002), (200), (112), (130), (202), (222), (312), and (242) planes, respectively, and match very well with the standard card (JCPDS 48-0898) of the standard of an orthorhombic $InVO_4$ catalyst; one can deduce that the sample were of orthorhombic crystal structure. All prepared IVCS samples showed diffraction patterns that were consistent with the orthorhombic phase (JCPDS card no. 48-0898). Compared to the peaks seen in pure $InVO_4$, CdS XRD patterns of CdS-doped $InVO_4$ samples showed no additional diffraction peaks. This challenges the possibility of impurity phase production due to CdS and $InVO_4$ chemical interactions. No other crystalline peaks from impurity materials such as $In(OH)_3$, V_2O_5, and In_2O_3 were observed. The hydrothermally prepared counterpart $InVO_4$ could be indexed to a pure orthorhombic phase (JCPDS 48-0898) of $InVO_4$ [Figure 1A(b)]. As coupling these two semiconductors, in $InVO_4$-CdS heterojunction materials, similar diffractions to the pure CdS and $InVO_4$ are observed, indicating that the heterogeneous process would not bring any influence on the crystal structure [Figure 1A(c)]. In $InVO_4$-CdS heterojunction materials with different weight percentages of CdS content, the diffraction peak intensities of CdS increased remarkably with increasing concentration of precursors content (Figure 1B). When compared with pure $InVO_4$ and CdS samples, the interplanar spacing of the (112) orthorhombic crystallographic plane of the CdS-doped samples increased. This indicates that Cd^{2+} ions have been replaced into the orthorhombic $InVO_4$ lattice. As a result, CdS insertion encouraged the distorted state of the $InVO_4$ materials' crystalline structure.

The morphologies of CdS, $InVO_4$, and $InVO_4$-CdS were characterized by field-emission scanning electron microscopy (FESEM) and transmission electron microscopy (TEM) analysis. Figure 2a−d shows the FESEM images of $InVO_4$-CdS at 10 K magnifications IVCS-1, IVCS-2, IVCS-3, and IVCS-5 respectively.

The $InVO_4$-CdS catalysts show aggregated microrods and a microflower morphology with a size of around 2 μm. The $InVO_4$-CdS are small, highly crystalline nanoparticles that are attached and self-assembled to form a microflower (Figure 2b). In the case of the $InVO_4$-CdS composite, the surface morphology of the heterostructured $InVO_4$-CdS closely resembles that of pure $InVO_4$. The CdS component of the composite, which consists of a combination of microrods and microflowers, is only minimally noticeable on the $InVO_4$ microrod due to the relatively low concentration of CdS. In the preparation of $InVO_4$-CdS catalysts, sulfide ions ($S^{2−}$) can be released more rapidly from the thioacetamide solution mixture at higher temperatures during the hydrothermal method (220 °C). A greater quantity of sulfide ions in a thioacetamide solution progressively enhances the nucleation and growth rates of CdS nanocatalysts in $InVO_4$-CdS. The formation mechanism of CdS spheres in $InVO_4$-CdS can be attributed to the spontaneous Ostwald ripening process. The
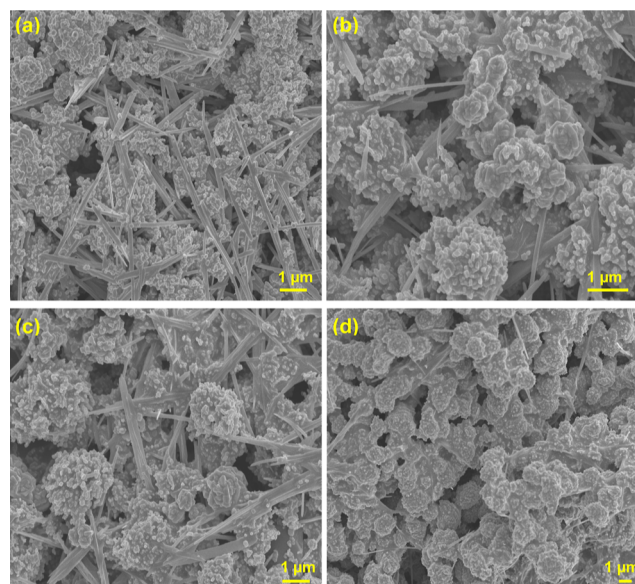
Figure 2. FESEM images of $InVO_4$-CdS at 1 μm and 10 K magnifications: (a) IVCS-1, (b) IVCS-2, (c) IVCS-3, and (d) IVCS-5.

formation of microflowers increases as the concentration of CdS on $InVO_4$ increases.

The formation of heterostructured $InVO_4$-CdS was further confirmed by the elemental color mapping images shown in Figure 3. Elemental maps of In−L, V−K, O−K, Cd−L, and S−K have a mixture of microrods and microsphere shapes and are placed in the catalyst materials, which proves the presence of $InVO_4$ and CdS in the as-fabricated composite. This provides solid proof of the formation of heterostructured $InVO_4$-CdS.
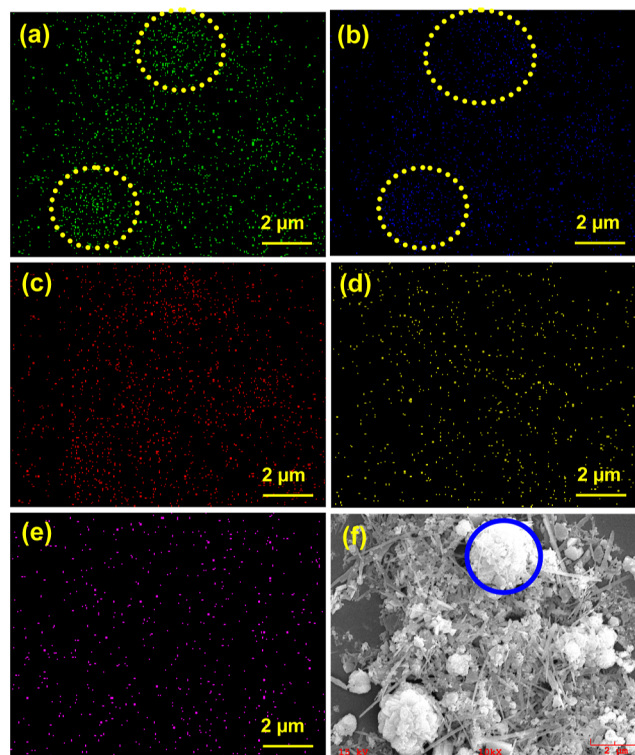
Figure 3. Elemental color mapping images of IVCS-3: (a) Cd, (b) S, (c) In, (d) V, and (e) O and (f) FESEM images of IVCS-3.

There is a homogeneous distribution of Cd, S, In, V, and O at uniform concentrations (Figure 3a−e). This also indicates the purity of the catalyst InVO$_4$-CdS. No other impurities are present in the catalyst materials.

To further determine the internal structural information on heterostructured InVO$_4$-CdS, the catalyst material was investigated by TEM, high-resolution transmission electron microscopy (HR-TEM), and selected area electron diffraction (SAED), as presented in Figure 4. Figure 4a,b shows a typical
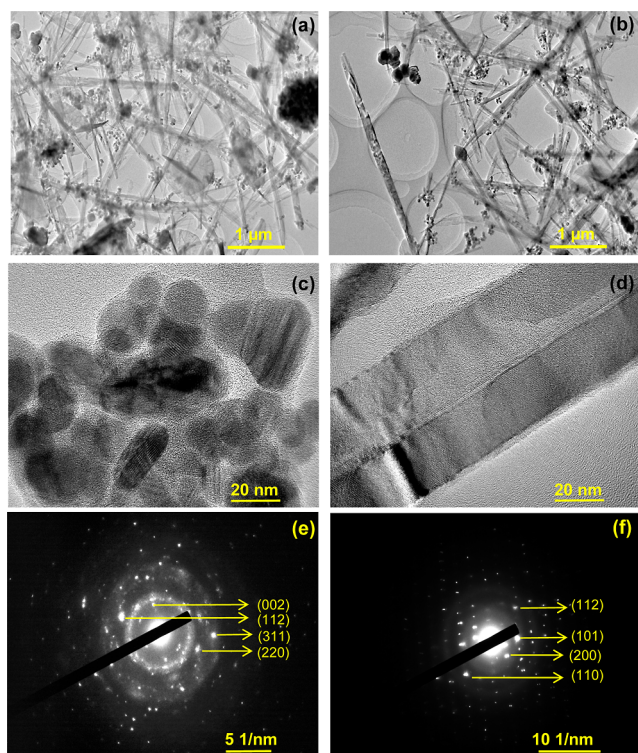
Figure 4. TEM images of IVCS-3 (a,b) particles and nanorod distribution at 1 μm, (c,d) HR-TEM images of nanoparticles and nanorod at 20 nm respectively, (e) SAED pattern of 5 1/nm, and (f) SAED pattern of 10 1/nm.

low-magnification TEM image of InVO$_4$-CdS, in which a series of irregular shapes like rods and very small nanoparticles can be observed on the projection framework because of the stacking of primary blocks (particles and rods). Interestingly, the corresponding SAED pattern (Figure 4c,d) recorded from the whole assemblies of nanoparticles (to self-assemble and form a microsphere) and microrods only present a single set of sharp diffraction spots in a rectangle and sphere arrangement, as found in Figure 4e,f. The diameter of the nanoparticles was about below 30 nm, the rods were below 20 nm, and length of the rods was 0.7−2.3 μm, although the nanoparticle and rods were highly crystalline. The presence of many tiny pores on the flat lamina may be attributed to the release of water and carbon dioxide molecules, as well as the structural deformation that occurs during the calcination process.[40] The SAED pattern and FFT images of the CdS microflower shown in Figure 4e reveal that the CdS in synthesized InVO$_4$-CdS heterostructures nanocrystals is polycrystalline in appearance. The concentric rings in the SAED pattern correspond to the (002), (112), (220), and (311) planes, respectively. SAED patterns correspond to the (112), (101), (200), and (110) planes of InVO$_4$ crystals (Figure 4f). The HR-TEM image (Figure 5b)
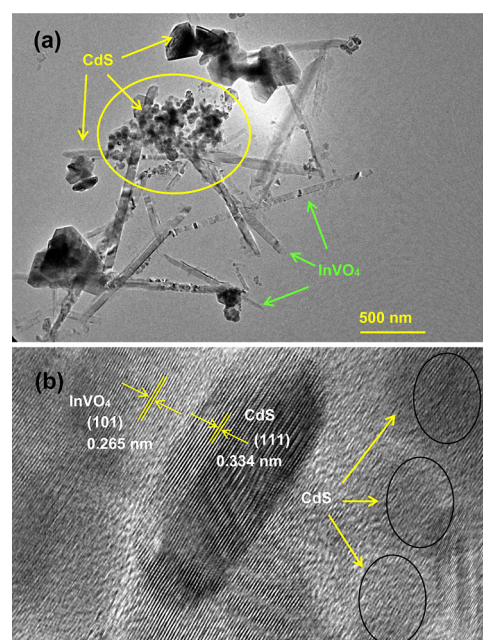
Figure 5. HR-TEM image of IVCS-3: (a) nanoparticles and nanorod distribution at 500 nm and (b) lattice fringes at 2 nm.

shows a perfect lattice fringe, which demonstrates the polycrystalline nature of the spheres and crystalline rods, and resolved interplanar spacing distances are about 0.344 and 0.291 nm which correspond to the d values of the (220) and (021) crystallographic facets of orthorhombic InVO$_4$, respectively.[41] The lattice fringes of CdS in the InVO$_4$-CdS composite show interplanner distances of 0.352, 0.336, and 0.316 nm, which is appropriate to the (100), (002), and (101) planes of hexagonal CdS, respectively.[42] TEM images of pure InVO$_4$ and CdS are given in the Supporting Information (Figure S1). From these images, we can distinguish the shapes of InVO$_4$ and CdS. InVO$_4$ shows a nanorod-like morphology, and CdS small particles make cluster-like structures. Due to the hydrothermal, drying and calcination processes, the preparation materials show agglomeration (using high temperatures-220 °C at 24 h). This observation is consistent with the XRD result. This result confirms the coexistence of InVO$_4$ and CdS nanocrystal materials. The strong interconnection between semiconductors seen in this study demonstrates promising potential for facilitating charge transfer between InVO$_4$ and CdS, thereby promoting the effective separation of photogenerated carriers (h$^+$ and e$^-$) and augmenting the photocatalytic activity.[43] The interfacial linkages between InVO$_4$ and CdS are abundantly evident in the lattice fringes seen in the photos.

To find out the optical properties, UV−vis diffuse reflectance and photoluminescence (PL) spectra for the InVO$_4$-CdS, InVO$_4$, and CdS catalysts were recorded (Figure 6). The UV−visible diffuse reflectance spectra are analyzed to further evaluate the growth of an InVO$_4$-CdS microflower. In Figure 6A(c), it is evident that the InVO$_4$-CdS sample does exhibit a pronounced absorption band in the UV−visible spectrum. Because of the nano size impact of the CdS nanoparticles, the absorption edge of the InVO$_4$-CdS sample has been shifted blue by approximately 87 and 17 nm when compared to the bulk CdS (612 nm) and InVO$_4$ microrods, respectively, in Figure 6A(a,b). InVO$_4$-CdS shows an increased
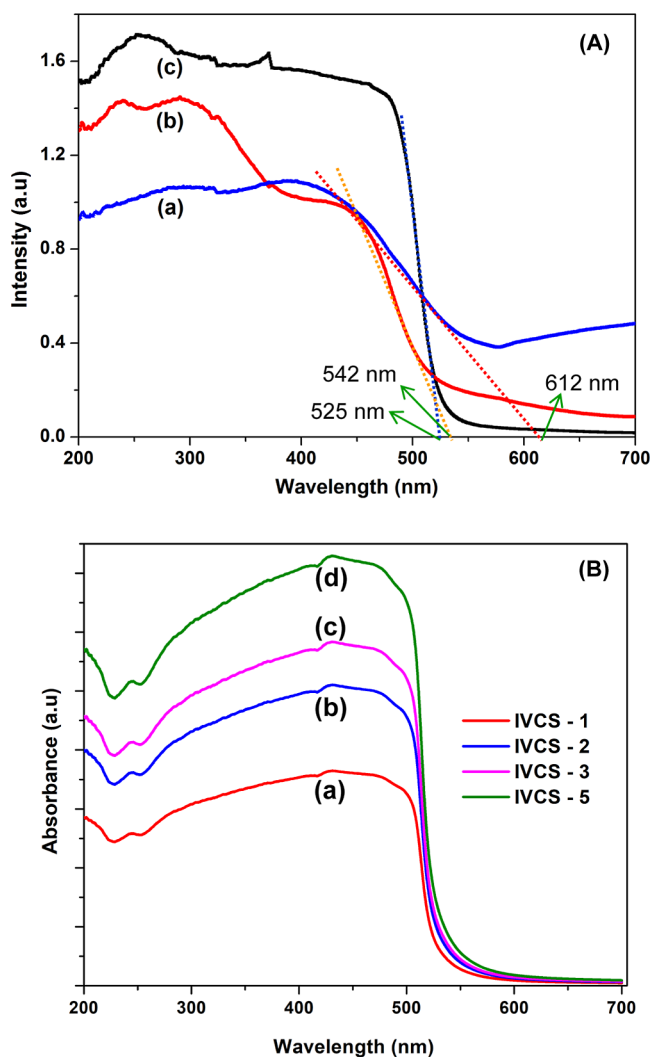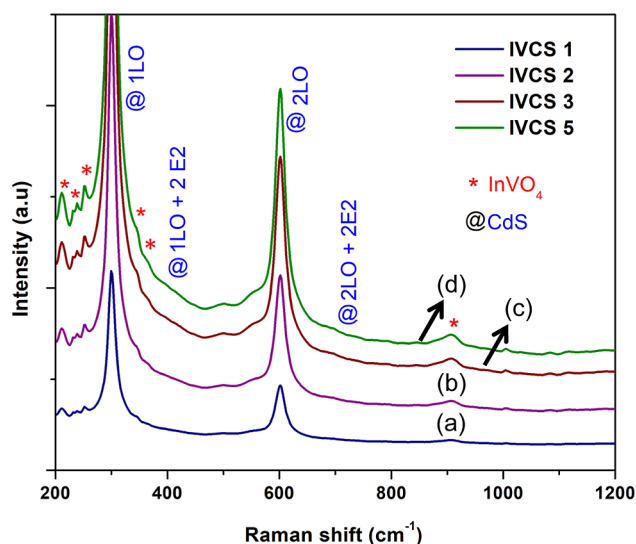
Figure 6. UV−vis DRS of (A) (a) prepared CdS, (b) prepared InVO$_4$, and (c) IVCS-3. (B) Different concentrations of InVO$_4$-CdS: (a) IVCS-1, (b) IVCS-2, (c) IVCS-3, and (d) IVCS-5.

Figure 7. Raman spectra of (a) IVCS-1, (b) IVCS-2, (c) IVCS-3, and (d) IVCS-5.

absorption over the undoped InVO$_4$ and CdS material in both the visible and ultraviolet regions (Figure 6). The increase in the concentration of CdS in the InVO$_4$ absorption edge has been red-shifted. UV−vis spectra in the diffuse reflectance mode (R) were transformed to the Kubelka−Munk function $F(R)$ to separate the extent of light absorption from scattering. The band gap energy was obtained from the plot of the modified Kubelka−Munk function $[F(R)E]^{1/2}$ versus the energy of the absorbed light E (eq 1)

$$F(R)E^{1/2} = \left[\frac{(1-R)^2}{2R} \times h\nu \right]^{1/2}$$

(1)

The band gap energies of InVO$_4$-CdS, InVO$_4$, and CdS are reported to be 2.43, 2.52, and 2.26 eV, respectively. The presence of defects inside the semiconductor oxide material may give rise to intermittent band energy levels, resulting in a reduction of the band gap energy. Consequently, this reduction in band gap energy results in an increase in UV−visible absorption.

Raman spectroscopy was used to describe the InVO$_4$-CdS nanocomposite's structure and electronic characteristics (Figure 7a−d). The orthorhombic phase of InVO$_4$ is responsible for the bands seen at 207, 312.8, 377.2, and 928 cm^{-1}. An about 900 cm^{-1} V−O stretching mode and an 800−600 cm^{-1} V−O−V and V−O−In stretching are seen in the Raman spectra, respectively. The laser-Raman spectra indicate that the peaks observed at 860 and 782 cm^{-1} correspond to the A1g symmetric (ν1) and B1g asymmetric (ν3) stretching modes of the V−O tetrahedron, respectively.[44] Furthermore, the peaks situated at 465 (B1g) and 375 cm^{-1} (A1g) are associated with the characteristic bending modes of InVO$_4$.[45] The ν2 (B2g) bending mode of V−O tetrahedrons is seen at a frequency of 258 cm^{-1}, whereas the peak at 228 cm^{-1} is identified as the B1g bending mode of V−O vibration.[46] The stretching modes of the V−O bonds are represented by the peaks seen at 207, 312, and 377 cm^{-1}, as shown in Figure 7. Additionally, the peak observed at 911 cm^{-1} is attributed to the vibration of In−O bonds in InVO$_4$.[34] Additionally, there are peaks seen at wavenumbers of 300, 600, and 900 cm^{-1}, which may be attributed to the phonon vibrational modes of 1LO, 2LO, and 3LO in hexagonal CdS microflowers, respectively. One of the observed vibrations is the A1 mode, which generates a peak at 300 cm^{-1}, corresponding to the Cd−S bond. Based on the graphical representation, it is evident that the intensity of the peak at 900 cm^{-1} is much lower compared to that of the other two peaks. Additionally, the Raman vibration peak corresponding to 3LO typically has a reduced intensity. In this discussion, we just focus on the vibration peaks associated with the first overtone (1LO) and second overtone (2LO).[47] The Raman spectra of pure InVO$_4$ and CdS are presented in Figure S2.

To study the efficiency of transferring charge carriers in semiconductors, which may reflect the splitting and recombination of photoexcited electron−hole pairs, PL spectroscopy is often utilized. A decrease in PL emissions is often associated with an increase in separation efficiency and a decrease in the rate of charge carrier recombination. The PL spectrum of CdS-doped InVO$_4$, as shown in Figure 8, exhibits the least PL intensity. In contrast, the emission intensity of pure InVO$_4$ exhibited a somewhat higher magnitude. Based on the prior studies, it can be inferred that the inclusion of InVO$_4$ and CdS has the potential to effectively augment the rate of separation between photoinduced electrons and hole pairs, generate a
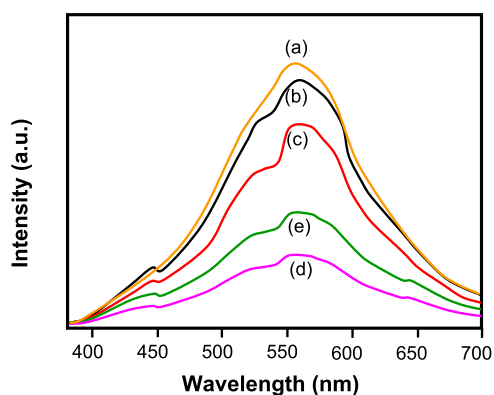
Figure 8. PL spectra of (a) prepared InVO$_4$, (b) IVCS-1, (c) IVCS-2, (d) IVCS-3, and (e) IVCS-5.

greater number of active species, and thus improve the performance of the photocatalytic process.[48] By eliminating organic molecules, reactive species like h$^+$, OH$^-$, and O$_2^-$ greatly influence the photocatalytic activity.

X-ray photoelectron spectroscopy (XPS) analysis is used to determine the oxidation state and elemental composition for every element of the InVO$_4$-CdS heterojunction (Figure 9a–f). The high-resolution XPS spectra of In 3d, V 2p, O 1s, Cd 3d, and S 2p for InVO$_4$-CdS are given in Figure 9b–f. Figure 9b displays that two peaks at binding energy (BE) values of 445.1 and 452.6 eV and are assigned to the In 3d$_{5/2}$ and In 3d$_{3/2}$ signals of In^{3+} species, respectively. This is consistent with the results of the other XPS in InVO$_4$-CdS.[49,50] The BE of In 3d$_{5/2}$ in the obtained InVO$_4$-CdS is greater than that of element indium, suggesting that the indium atoms in the hydrothermally prepared catalysts are positively charged by the formation of direct bonds with oxygen.[51] The V 2p core level spectrum is shown in Figure 9c. The main BE peaks for V 2p$_{3/2}$ and V 2p$_{1/2}$ were present at 517.3 and 524.8 eV, respectively, and corresponded to the V^{5+} oxidation state in InVO$_4$ (Figure 9c).[52] The O 1s profile of O 1s is asymmetric and can be fitted to two symmetrical peaks α and β located at 530.8 and 532.8 eV, respectively, indicating two different kinds of O species in the sample (Figure 9d). The BE peaks seen in Figure 9e, specifically the Cd 3d$_{5/2}$ and Cd 3d$_{3/2}$ peaks, are located at 405.6 and 412.3 eV, respectively. These peaks exhibit a spin–orbit separation of 6.7 eV. Based on these observations, it can be concluded that these peaks correspond to the presence of Cd^{2+} ions in CdS. This assignment is in agreement with previously published values. The existence of the sulfide species S^{2-} may be inferred from the observation of two signals, S 2p$_{1/2}$ and S 2p$_{3/2}$, with binding energies of 162.6 and 162.1 eV, respectively (Figure 9f). The confirmation of the occurrence of S2 may be inferred from the observed energy split of 1.4 eV between S 2p$_{3/2}$ and S 2p$_{1/2}$.[53] The elemental composition of InVO$_4$-CdS − 3 is presented in the Supporting Information (Table S1). From the analysis, the atomic percentage of In 3d (20.16%), V 2p (10.29%), O 1s (21.45%), Cd 3d (16.77%), and S 2p (5.41%), respectively, can be figured out.

The N$_2$ adsorption and desorption on the prepared InVO$_4$-CdS compound's surface were used for estimating the surface characteristics of the synthesized materials to be consistent with the Brunauer–Emmett–Teller (BET) theory of multi-layer adsorption and desorption (Figure 10). All prepared materials had a type-(IV) N$_2$ adsorption–desorption isotherm,

indicating that they were mesoporous materials.[54,55] The BET insights showed that the surface area of CdS was 16.115 m^2/g, that of InVO$_4$ was 24.291 m^2/g, and that of InVO$_4$-CdS was 62.714 m^2/g. The incorporation of CdS particles into the InVO$_4$-CdS composite results in a larger BET-specific surface area compared to pure CdS and InVO$_4$ which is significant for enhancing the composite's catalytic effectiveness. Highly dispersed CdS nanoparticles on an InVO$_4$ matrix show that their structure is excellent in preventing the nanoparticles from aggregating. The strong photocatalytic activity of the InVO$_4$-CdS nanocomposite could have been partly attributed to the sample's large specific surface area. The mesopore size distribution determined by the Barrett, Joyner, Halenda (BJH) approach is about 1.85 nm, as shown in the BJH plot for InVO$_4$-CdS nanocomposite in Figure 10.[56,57]

3.1. Photocatalytic Activity of the Nanostructured InVO$_4$-CdS. Figure 11 shows the photocatalytic degradation of AV 7 (5 × 10^{-4} M) under various experimental circumstances. The dye exhibits resistance to self-photolysis. In a similar experimental setup, including InVO$_4$-CdS, a significant reduction (23%) in the concentration of the dye was found under dark conditions. The observed phenomenon may be attributed to the adsorption of dye molecules onto the catalyst surface. AV 7 experiences a degradation rate of 99.6% when exposed to visible light irradiation for 60 min in the presence of InVO$_4$-CdS. However, when InVO$_4$ and CdS were made and tested, they exhibited degradation rates of 70.1 and 78.6%, respectively, during a 60 min time frame. The results indicate that InVO$_4$-CdS exhibits superior efficiency in AV 7 degradation compared to other photocatalysts, as shown in Figure 11B. The findings indicate that the increased photocatalytic efficiency seen in InVO$_4$-CdS may be attributed to the presence of the CdS dopant. The findings indicate that the catalyst has a high efficacy in the breakdown of azo dyes.

The results shown in Figure 12a provide evidence that the pH value of the dye solution has a substantial impact on the effectiveness of the organic moiety's degradation over visible light illumination. The pH of the solution was modified within the range of 3−11 by the introduction of equimolar amounts of hydrochloric acid (HCl) and sodium hydroxide (NaOH) before the commencement of light exposure. The use of a catalyst with a broad pH range for photocatalytic activity might provide significant benefits in the treatment of industrial effluent since the attainment of optimum photocatalytic efficiency cannot be achieved at certain pH levels. The effectiveness of the synthesized InVO$_4$-CdS in photocatalysis over a wide range of pH values is seen in Figure 12a, indicating that it could be employed in the remediation of industrial wastewater. The photocatalyst such as InVO$_4$-CdS exhibits superior efficiency throughout the neutral pH range, demonstrating a degradation rate of 99.1%. This surpasses the effectiveness of both the InVO$_4$ and CdS photocatalysts. The presence of H$^+$ and OH$^-$ ions in dye solutions leads to a decrease in efficacy, seen under both acidic and basic conditions. The aforementioned ions possess the capacity to hinder the assimilation of the organic constituent present on the surface of the InVO$_4$-CdS catalyst. Metal vanadate and sulfide catalysts often exhibit unique active sites on their surfaces that promote the appearance of possible reactions. The pH of the dye solution has an impact on the surface charge of both the catalyst and AV 7 dye molecules. The adsorption behavior of dye molecules on the surface of InVO$_4$-CdS photocatalysts is influenced by the pH-dependent
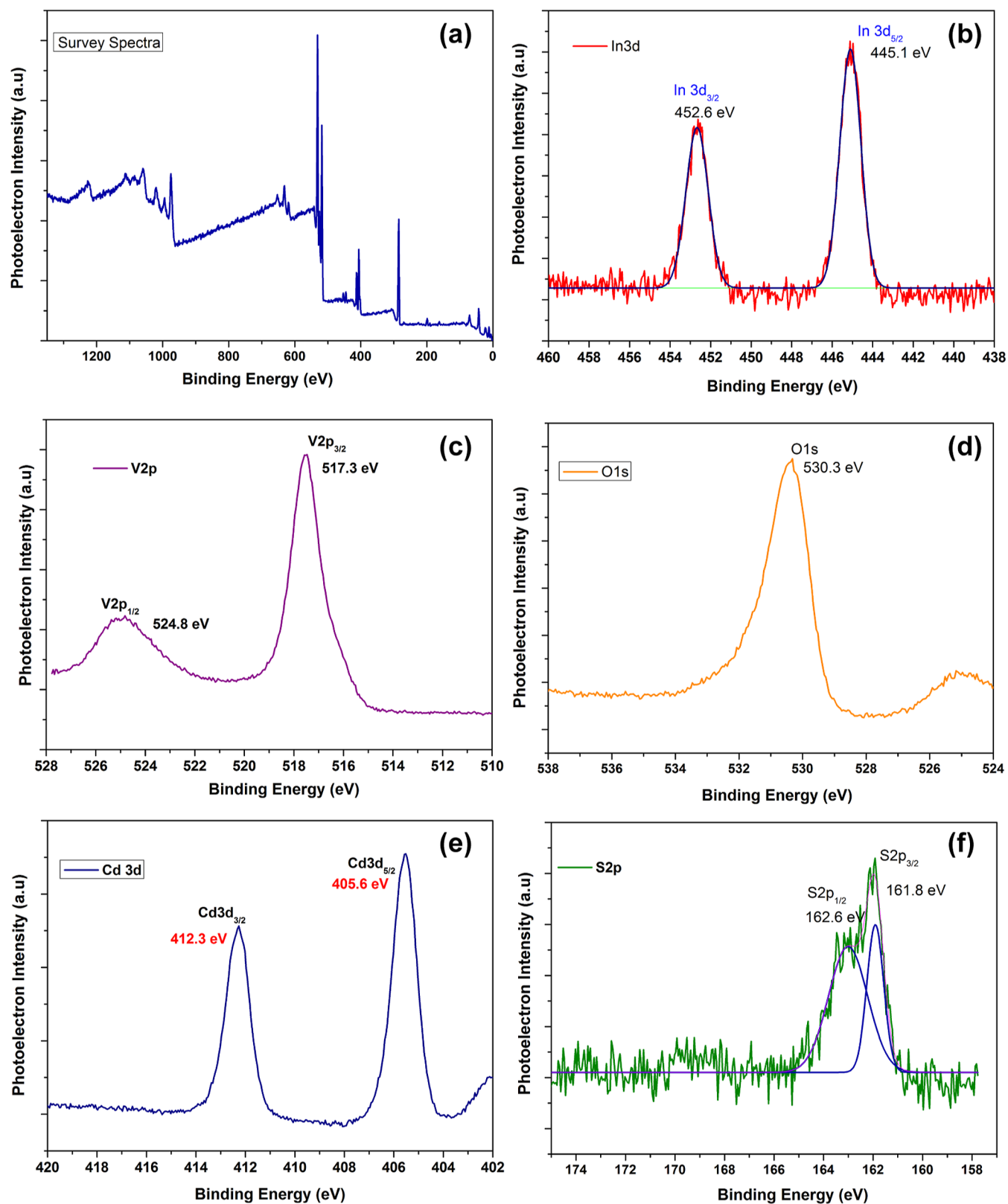
Figure 9. XPS spectra of InVO$_4$-CdS: (a) survey spectra, (b) In 3d, (c) V 2p, (d) O 1s, (e) Cd 3d, and (f) S 2p.

fluctuations in the surface charge of the heterostructured material. Anionic reactants tend to adsorb on catalyst surfaces that are positively charged, whereas cationic reactants show a higher propensity to adsorb on surfaces that are negatively charged. Metal oxides often exhibit hydroxyl groups (OH$^-$) on their surfaces, which might potentially act as either acidic or basic entities. The hydroxyl groups may undergo protonation or deprotonation. The existence or absence of certain acidic or basic sites may have an influence on the reaction pathways. The technique of protonation may be required in certain
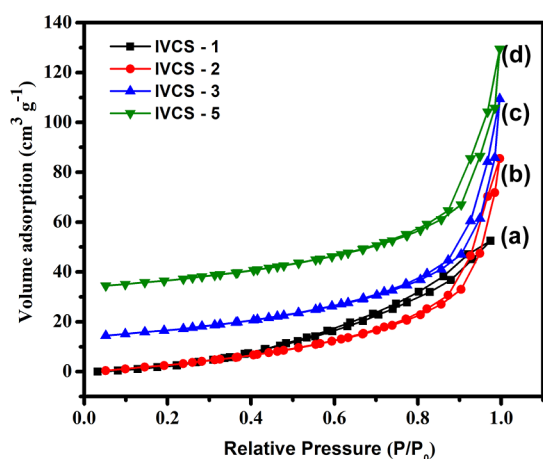
Figure 10. N$_2$ adsorption−desorption isotherms of (a) IVCS-1, (b) IVCS-2, (c) IVCS-3, and (d) IVCS-5.
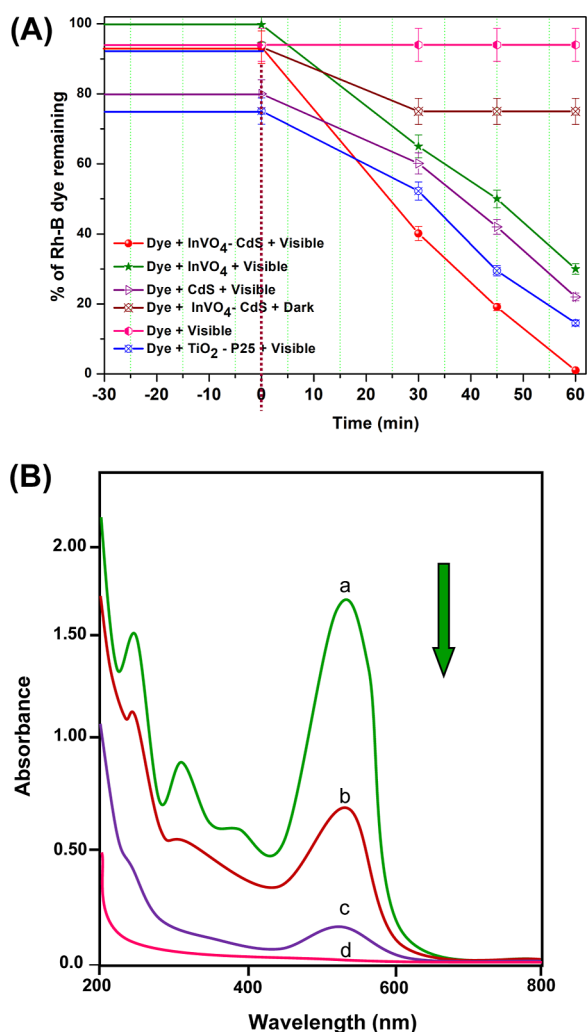
Figure 11. (A) Primary analysis of AV 7 dye degradation using different catalysts, dye concentration = 5×10^{-4} M; p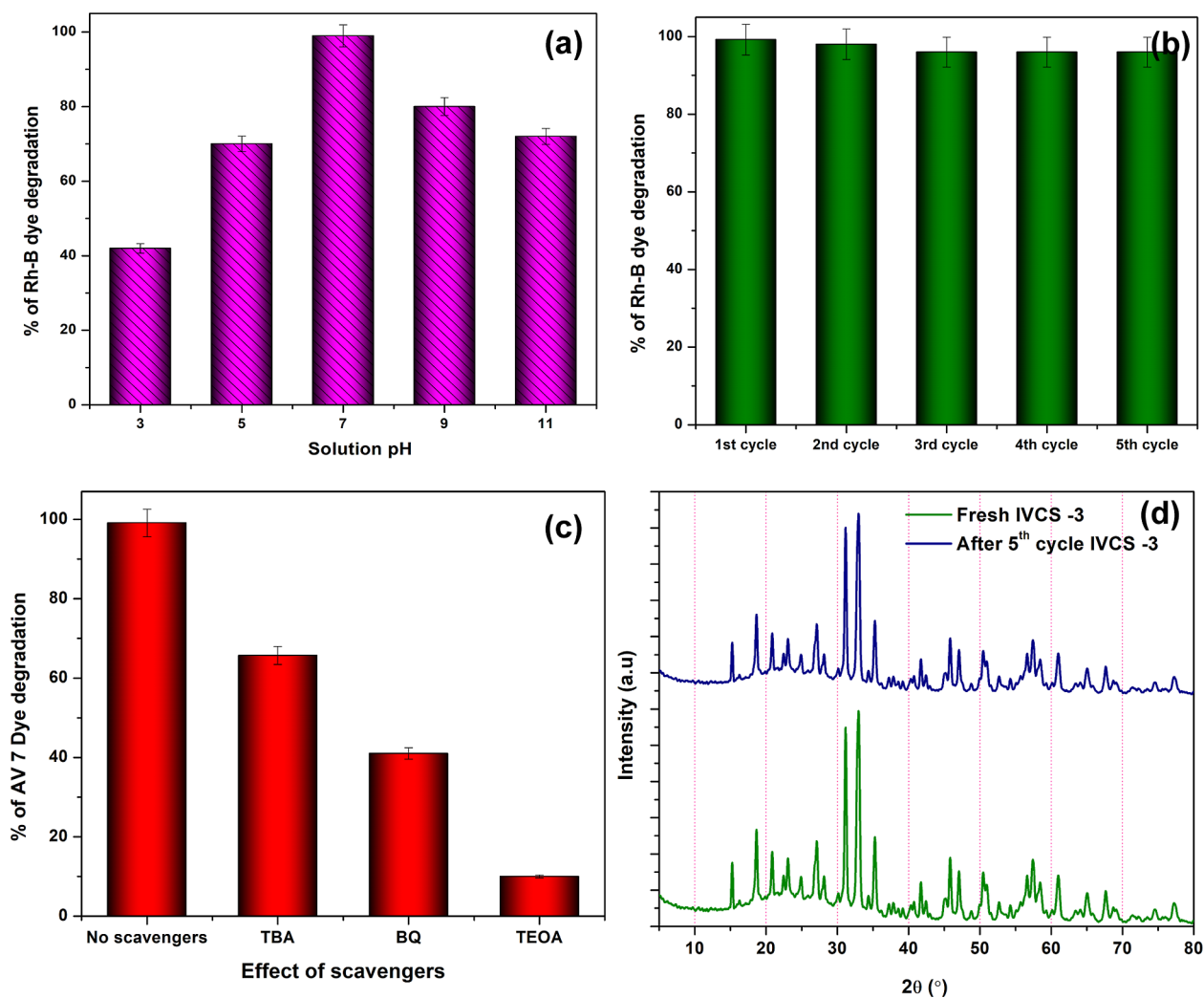H = 7, catalyst suspended = 3 g L^{-1}, airflow rate = 8.1 mL s^{-1}, $I = 1.381 \times 10^{-6}$ einstein L^{-1} s^{-1}, and irradiation time = 60 min and (B) AV 7 Dye degradation of spectra using IVCS-3 at different intervals: (a) 0, (b) 30, (c) 45, and (d) 60 min.

interactions between the catalyst and the reactants. Ionic associations between charged species in dye solutions and the InVO$_4$-CdS surface have the potential to modify adsorption and reaction rates. The redox (oxidation−reduction) process plays a crucial role in facilitating the efficacy of photocatalytic processes. The redox potential of a dye solution is influenced by its pH, which then impacts the accessibility of electrons for redox reactions occurring on the surface of InVO$_4$-CdS. The catalytic efficiency may be diminished by the presence of H$^+$ ions, which may prevent the production of OH• radicals. The percentage of degradation exhibits an upward trend when the pH transitions from acidic to neutral, followed by a further decline until it stabilizes at pH 11. The target of maintaining a neutral pH was consistently maintained throughout the experiment, since it was shown to provide the highest level of activity. The breakdown efficiency of dye molecules employing the InVO$_4$-CdS photocatalyst is much higher in comparison to that of pure InVO$_4$ and CdS. Subsequently, the energized electrons and holes have the potential to participate in redox reactions with molecules that have undergone adsorption onto the surface of the catalyst. The interaction between holes and excited electrons may facilitate the breakdown of adsorbed organic molecules, leading to the fragmentation of these molecules into smaller, less-harmful chemical species. InVO$_4$-CdS induced modifications in the energy levels of the VB and CB, enhanced the surface area available for adsorption, and facilitated charge separation. The aforementioned alterations may potentially impact the photo-catalytic efficacy of the material. Presented below is a schematic representation of the suggested photodegradation pathway for the photocatalyst used in the degradation of AV 7 dye during treatment. (1) The absorption of visible light by a photocatalyst results in the generation of electron−hole pairs, with the holes being located in the VB and the electrons occupying the CB. Holes experience oxidation, resulting in the generation of hydroxyl radicals (OH•). (2) Electrons engage in a reduction process whereby they mix with atmospheric oxygen to generate superoxide radical anions (O$_2$), which then transform into hydrogen peroxide (H$_2$O$_2$), and ultimately result in the formation of hydroxyl radicals (OH). The active radicals generated during the process catalyze the decom-position of organic contaminants, resulting in the formation of benign molecules, namely, water (H$_2$O) and carbon dioxide (CO$_2$).

The reusability of InVO$_4$-CdS was tested for the degradation of the AV 7 dye under an indistinguishable reaction environment. After complete degradation, the catalyst was separated and washed with the huge amount of deionized water. The recovered catalyst was dried in a hot air oven at 100 °C for 3 h and used for a second run. Figure 12b shows the outcome of the AV 7 dye degradation for five runs. InVO$_4$-CdS exhibits notable photostability as the AV 7 dye degradation percentages are 99.6, 98.2, 96.0, 96.0, and 96.0 for 60 min in the first, second, third, fourth, and fifth runs, respectively. There is no considerable change in the degradation efficiency of InVO$_4$-CdS after five runs.

Trapping studies for AV 7 dye degradation over InVO$_4$-CdS were used to study the primary reactive species to understand the photocatalytic process. When AV 7 dye was photocatalyti-cally decomposed under the influence of visible light, several quenchers were introduced. In this instance, hydroxyl radical (OH$^-$), superoxide radical (O$_2^-$), and hole (h$^+$) scavengers were used in the amounts of 2 mM TBA, 2 mM benzoquinone,

Figure 12. (a) Effect of AV 7 dye solution: pH dye concentration = 5×10^{-4} M, catalyst suspended = 3 g L^{-1}, airflow rate = 8.1 mL s^{-1}, (b) cycle stability of InVO$_4$-CdS heterostructure for AV 7 dye degradations, (c) effect of scavengers on the photodegradation of AV 7 under visible light over InVO$_4$-CdS, and (d) cycle stability of fresh and after fifth cycle reusable catalyst XRD pattern.

Scheme 2. Photocatalytic Degradation Mechanism of AV 7 Dye Using IVCS-3
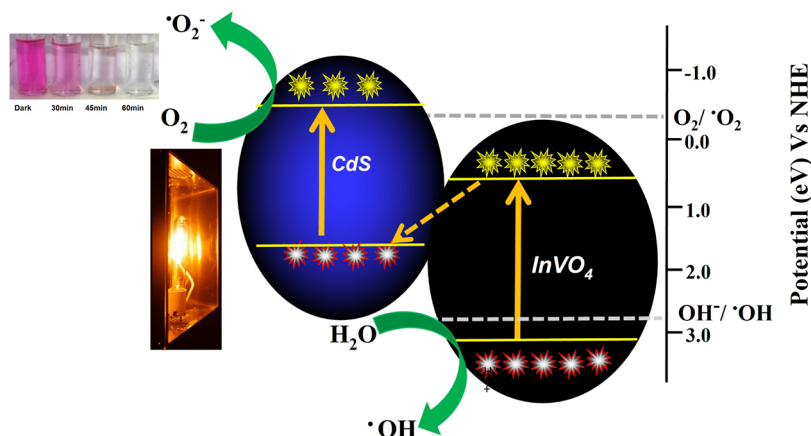
and 2 mM TEOA. When BQ was introduced, the photocatalytic activity of 1.0 mol % CdS-functionalized InVO$_4$ significantly reduced, suggesting that superoxide anion radicals, as opposed to hydroxyl radicals or photoinduced holes, were the main active component for AV 7 dye photodegradation (Figure 12c). TEOA was used as a scavenger for h$^+$,[58−60] p-

benzoquinone was utilized as a scavenger for •O$_2$$^-$,[51,52] and TBA was employed as a scavenger for OH•.[61,62] Figure 12c illustrates the observed suppression of photodegradation of the AV 7 dye over InVO$_4$-CdS by all scavengers. The suppression of AV 7 dye photodegradation was seen when TEOA and p-BQ were present, indicating that h$^+$ and •O$_2$$^-$ played a more

Scheme 3. Degradation Pathway of AV 7 Dye

$OH^\bullet + O_2^{\bullet-}$

(1) M⁺ = 206.7

2,8-diaminonaphthalene-1,3,6-triol

$OH^\bullet + O_2^{\bullet-}$

(2) M⁺ = 207.4

2-aminonaphthalene-1,3,6,8-tetraol

Repetitive attack of
$OH^\bullet + O_2^{\bullet-}$

2-aminobenzene-1,3-diol
(3) M⁺ = 125.4

5-aminobenzene-1,3-diol
(4) M⁺ = 125.6

2-aminobenzene-1,4-diol
(5) M⁺ = 125.1

Repetitive attack of
$OH^\bullet + O_2^{\bullet-}$

$CO_2 + H_2O$ + Mineral acids
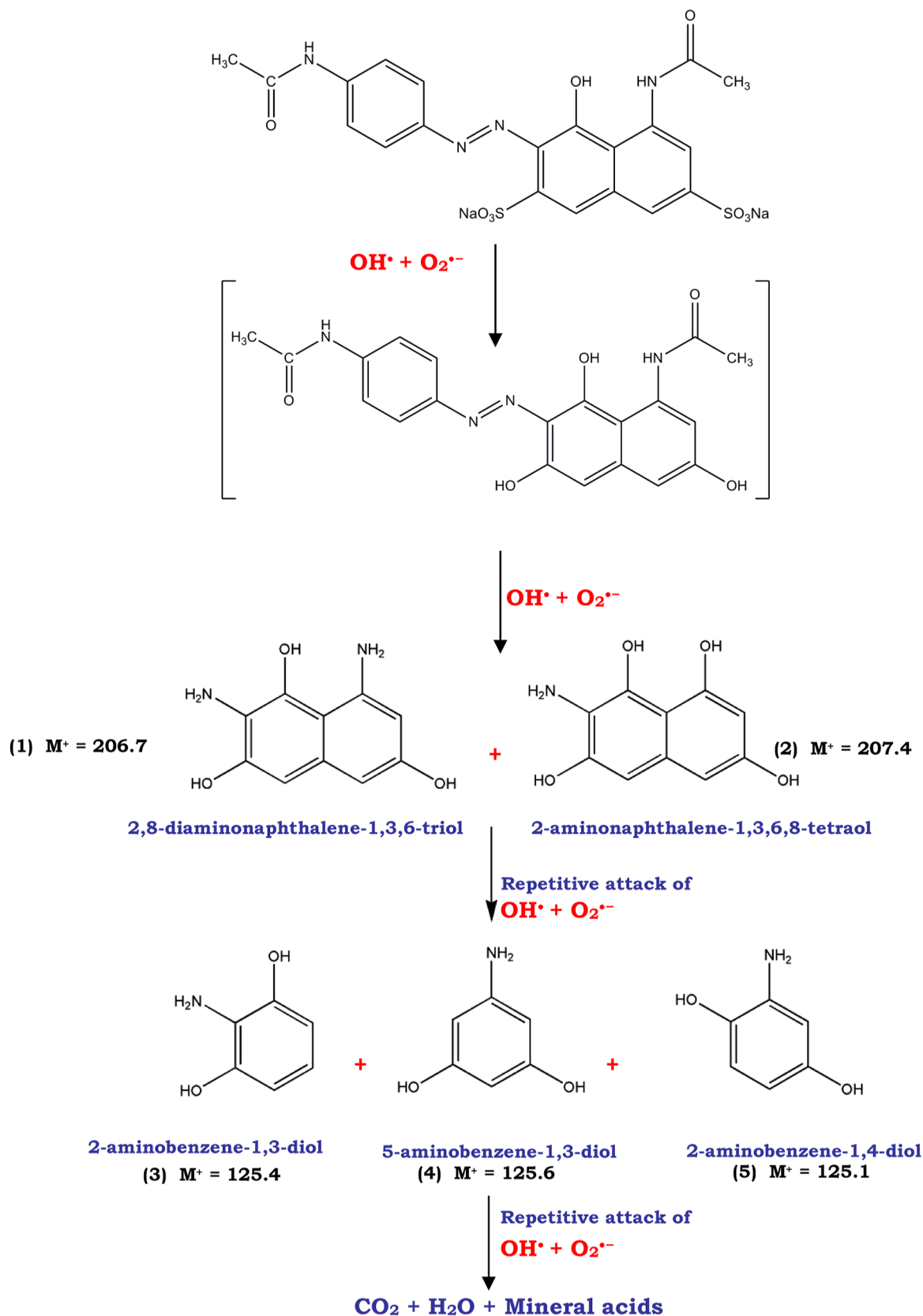
prominent role in the photodegradation mechanism. A potential mechanism for the decomposition of the AV 7 dye over InVO₄-CdS under visible light is hypothesized and shown in Scheme 2, taking into account the trapping experiments and band edge placements. The energy band gaps of InVO₄ and CdS are reported to be 3.25 and 2.6 eV, respectively. Additionally, the energy levels of the CB minimum (ECBM) and VB maximum (EVBM) for InVO₄ are recorded as 0.61

and 3.17 eV, respectively. Similarly, for CdS, the ECBM and EVBM values are −0.6 and 1.56 eV, respectively.[58] To produce superoxide radicals, it is necessary for the ECBM of a semiconductor to have a greater negative value than −0.046 eV, which is the standard reduction potential ($E0$) of $O_2/\bullet O_2^-$ relative to the normal hydrogen electrode.[63]
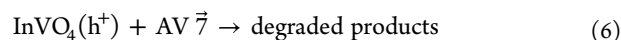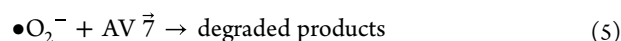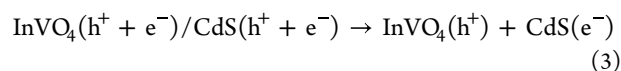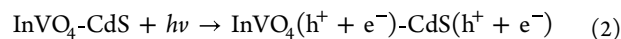
Based on the results mentioned earlier and further research, a plausible mechanism has been postulated to elucidate the augmented photocatalytic efficacy shown by the InVO4-CdS heterojunctions. The charge-transfer mechanism in InVO4-CdS is an essential characteristic of its photocatalytic properties. The pathway relies on the interaction between two distinct semiconductors, InVO4 and CdS, which possess differing band gap energies. On illumination to visible light, the InVO4-CdS composite exhibits photon absorption, and the energy of these photons must be at least similar to the band gap of the appropriate semiconductor. The absorption of light leads the electrons in the VB to get excited and migrate to the CB. This mechanism creates electron−hole pairs in both InVO4 and CdS materials. The CB of CdS in the composite material often has a lower energy level compared with that of InVO4. The accurate placements of the band structures of CdS and InVO4 were precisely established by VB-XPS investigation. The VB potentials of CdS and InVO4 were determined to be 1.56 and 3.17 eV, respectively, as shown in Scheme 2. The VB CB potentials of synthesized CdS and InVO4 were established by calculating them to be −0.66 and 0.61 eV, accordingly (Scheme 2). With the CB edge of InVO4 below −0.33 eV, reduction primarily occurs in the CdS CB. Simultaneously, oxidation predominantly occurs in the VB of InVO4. The proposed mechanism aligns with findings in the literature, indicating that the composite materials adhere to the Z-scheme pathway depicted in the diagram.

Hence, the staggered band arrangement facilitates the efficient separation and transmission of photoinduced charge carriers. InVO4 has a greater energy level for its VB compared with CdS. The disparity in energy levels enables the exchange of charges between the two semiconductors. Electrons in an excited state inside the CB of CdS have the ability to move to the CB of InVO4. The transfer is thermodynamically favorable as a result of the lower energy state of the CB in InVO4 in comparison to CdS. Likewise, the vacancies in the VB of InVO4 might migrate to the VB of CdS. The transfer of electrons occurs due to the disparity in energy levels between the VB of CdS and InVO4, with CdS having a lower energy level. The isolated charge carriers are capable of engaging in redox processes. Electrons in the CB have the ability to catalyze the reduction of dye molecules. VB vacancies have the ability to oxidize things, such as breaking down organic contaminants. The charge separation and transfer method used in this system effectively reduce the recombination rate of electron−hole pairs, a prevalent challenge encountered in single-semiconductor photocatalysts. The effectiveness of the InVO4-CdS composite in photocatalytic applications is enhanced by the reduction of recombination.[64−66]

Upon irradiation with visible light, the InVO4-CdS composites exhibited the excitation of electrons (e^-) from the VB to the CB, resulting in the generation of holes (h^+) in the VB of each semiconductor. Due to the difference in the CB edge potentials between CdS and InVO4, the CB potential of CdS is greater than that of InVO4. Consequently, if electrons generated by photons are transported from the CB of CdS to the CB of InVO4, then the electrons in the CB of InVO4 would

be unable to create $\bullet O_2^-$ radicals. This is due to the more positive CB potential of InVO4. Hence, it is probable that the photogenerated electrons located in the CB of InVO4 would undergo transfer and recombination with the photogenerated holes positioned in the VB of CdS.

Thus, an increased number of electrons will gather in the CB of CdS, facilitating their interaction with surface-adsorbed oxygen (O_2) to produce a greater quantity of superoxide radicals ($O_2/\bullet O_2^- = -0.33$ eV). Subsequently, these active species ($\bullet O_2^-$) participate in the photocatalytic process. In the context of InVO4, the photogenerated holes present in the VB have a tendency to undergo direct reactions with AV 7 dye molecules. This reaction serves the objective of efficiently degrading AV 7 dye organic contaminants. Consequently, the Z-scheme InVO4-CdS heterojunctions were able to achieve efficient separation and migration of photogenerated electron−hole pairs, resulting in the acquisition of a robust redox capability for the photoexcited electron in the CB and the photoexcited hole in the VB, respectively. This phenomenon ultimately led to substantial improvements in the photocatalytic efficiency of the Z-scheme InVO4-CdS heterojunctions. The degradation of AV 7 dye using InVO4-CdS photocatalysts is explained in eqs 2−6.

$$InVO_4\text{-}CdS + hv \rightarrow InVO_4(h^+ + e^-)\text{-}CdS(h^+ + e^-) \quad (2)$$

$$InVO_4(h^+ + e^-)/CdS(h^+ + e^-) \rightarrow InVO_4(h^+) + CdS(e^-) \quad (3)$$

$$CdS(e^-) + O_2 \rightarrow \bullet O_2^- \quad (4)$$

$$\bullet O_2^- + AV\,\vec{7} \rightarrow \text{degraded products} \quad (5)$$

$$InVO_4(h^+) + AV\,\vec{7} \rightarrow \text{degraded products} \quad (6)$$

Through the use of gas chromatography−mass spectrometry (GC-MS) analysis of the AV 7 dye solutions that were obtained after 30 and 60 min of visible irradiation (Scheme 3), an effort has been made to determine the intermediate products that are developed during the photocatalytic degradation of AV 7 in InVO4-CdS during a process that is driven by visible light. The GC-MS analysis of the solution collected after 45 and 60 min revealed that the AV 7 dye had been photocatalytically degraded. We found that the retention time of the five prominent peaks ranged from 13.5, 31.29, 18.03, 19.89, and 23.04 min (Table 1). Products related to

Table 1. Molecular Ion and Fragmentation Peaks of AV 7 Dye

compound	retention time (min)	mass spectral data (m/z)
1	13.3	206.5 (M+) 191.4, 16.3, 57.0
2	31.5	207.1 (M^+) 138.6, 125.2, 97.5, 85.0, 57.2
3	18.6	125.3 (M^+) 110.6, 97.5, 83.4, 69.3, 57.2
4	19.1	125.7 (M^+) 110.6, 97.5, 83.4, 69.3, 57.2
5	23.8	125.4 (M^+) 110.6, 97.5, 83.4, 69.3, 57.2

these peaks were identified as 2,8-diaminonaphthalene-1,3,6-triol (1), 2-aminonaphthalene-1,3,6,8-tetraol (2), 2-amino-benzene-1,3-diol (3), 5-aminobenzene-1,3-diol, (4) or 2-aminobenzene-1,4-diol (5) based on their molecular ion and mass spectrometric fragmentation peaks. The components (3), (4), and (5) of the chemical could not be differentiated.

4. CONCLUSIONS

In summary, we have successfully achieved the controlled synthesis of $InVO_4$-CdS heterojunction photocatalysts using a combination of hydrothermal and hydrothermal decomposition strategies. The composites developed in this study showed a significant enhancement in photocatalytic performance compared to pure $InVO_4$ and CdS for the degradation of AV 7 dye upon exposure to visible light. Furthermore, the IVCS materials comprising 3 wt % demonstrated the most notable catalytic effectiveness in the degradation of AV 7 dye, achieving a remarkable 99.1% degradation during 60 min. The observed increase in photocatalytic activity may be due to the presence of a Z-scheme heterojunction system, which facilitates the efficient separation and transmission of electron–hole pairs. During the photodegradation process, $InVO_4$-CdS is stable and may be recycled. Three types of photogenerated radicals— holes (h^+), hydroxyl ($OH^\bullet$), and superoxide ($O_2\bullet$)—are responsible for the degradation process in a photocatalytic system. In light of the above, $InVO_4$-CdS may be a good option for both photodegradation and mineralization of the AV 7 dye. In addition, the heterojunctions of $InVO_4$-CdS have shown a notable level of stability in the context of the degradation of organic contaminants for environmental detoxification applications.

■ ASSOCIATED CONTENT

ⓢ Supporting Information

The Supporting Information is available free of charge at https://pubs.acs.org/doi/10.1021/acsomega.3c08850.

> Characterization details for the analysis of $InVO_4$-CdS, photocatalytic degradation experimental procedure, elemental composition from XPS analysis, TEM image of pure $InVO_4$ and pure CdS, Raman spectra of prepared $InVO_4$ nanorods and CdS nanoparticles, XPS analysis of pure $InVO_4$ and pure CdS, photocurrent and EIS measurement for optimized material, effect of initial dye concentrations, biocompatibility of $InVO_4$-CdS, TOC analysis, and comparison of previously reported heterostructure materials (PDF)

■ AUTHOR INFORMATION

Corresponding Authors

Balachandran Subramanian − *Department of Physiology, Saveetha Dental College and Hospitals, Saveetha Institute of Medical and Technical Sciences, Saveetha University, Chennai 600 077 Tamil Nadu, India;* ⓞ orcid.org/0000-0003-4173-2032; Email: balachem13@gmail.com

Jayant Giri − *Department of Mechanical Engineering, Yeshwantrao Chavan College of Engineering, Nagpur 441110 Maharashtra, India;* Email: jayantpgiri@gmail.com

Feng Wang − *Beijing National Laboratory for Molecular Science, CAS Key Laboratory of Engineering Plastics, Institute of Chemistry, Chinese Academy of Sciences, Beijing 100190, China;* ⓞ orcid.org/0000-0002-1096-129X; Email: wangfeng0822@iccas.ac.cn

Mingshu Yang − *Beijing National Laboratory for Molecular Science, CAS Key Laboratory of Engineering Plastics, Institute of Chemistry, Chinese Academy of Sciences, Beijing 100190, China;* ⓞ orcid.org/0000-0001-9839-6004; Email: yms@iccas.ac.cn

Authors

Zhongshan Xu − *Beijing National Laboratory for Molecular Science, CAS Key Laboratory of Engineering Plastics, Institute of Chemistry, Chinese Academy of Sciences, Beijing 100190, China*

Kumaravel Jeeva Jothi − *Department of Physiology, Saveetha Dental College and Hospitals, Saveetha Institute of Medical and Technical Sciences, Saveetha University, Chennai 600 077 Tamil Nadu, India*

Emad Makki − *Department of Mechanical Engineering, College of Engineering and Islamic Architecture, Umm Al-Qura University, Makkah 24382, Saudi Arabia; Department of Ocean and Resources Engineering, School of Ocean and Earth Science and Technology, University of Hawaii at Manoa, Honolulu, Hawaii 96822, United States*

Selvamani Muthamizh − *Department of Physiology, Saveetha Dental College and Hospitals, Saveetha Institute of Medical and Technical Sciences, Saveetha University, Chennai 600 077 Tamil Nadu, India*

Dhilip Kumar Rajaiah − *Department of Civil and Environmental Engineering, University of Ulsan, Ulsan 44610, Republic of Korea*

Natarajan Prakash − *Division of Chemistry, Department of Science and Humanities, Saveetha School of Engineering, Saveetha Institute of Medical and Technical Sciences, Saveetha University, Thanadalam 600056 Tamil Nadu, India*

Nagarani Sandran − *Department of Environmental Engineering and Management, Chaoyang University of Technology, Taichung 41349, Taiwan*

Complete contact information is available at: https://pubs.acs.org/10.1021/acsomega.3c08850

Notes

The authors declare no competing financial interest.

■ ACKNOWLEDGMENTS

■ REFERENCES

(1) Malato, S.; Fernández-Ibáñez, P.; Maldonado, M. I.; Blanco, J.; Gernjak, W. Decontamination and Disinfection of Water by Solar Photocatalysis: Recent Overview and Trends. *Catal. Today* **2009**, *147* (1), 1−59.

(2) Kuvarega, A. T.; Krause, R. W. M.; Mamba, B. B. Nitrogen/Palladium-Codoped TiO_2 for Efficient Visible Light Photocatalytic Dye Degradation. *J. Phys. Chem. C* **2011**, *115* (45), 22110−22120.

(3) Oshikiri, M.; Boero, M.; Ye, J.; Zou, Z.; Kido, G. Electronic Structures of Promising Photocatalysts $InMO_4$ (M = V, Nb, Ta) and $BiVO_4$ for Water Decomposition in the Visible Wavelength Region. *J. Chem. Phys.* **2002**, *117* (15), 7313−7318.

(4) Orel, B.; Surca Vuk, A.; Opara Krašovec, U.; Dražič, G. Electrochromic and Structural Investigation of $InVO_4$ and Some Other Vanadia-Based Oxide Films. *Electrochim. Acta* **2001**, *46* (13−14), 2059−2068.

(5) Vuk, A. S.; Krašovec, U. O.; Orel, B.; Colomban, P. Electrochromic and Ex Situ IR and Raman Spectroelectrochemical Studies of Li_xInVO_4 Films Charged/Discharged in the 0. *J. Electrochem. Soc.* **2001**, *148* (6), H49.

(6) Ye, J.; Zou, Z.; Oshikiri, M.; Matsushita, A.; Shimoda, M.; Imai, M.; Shishido, T. A Novel Hydrogen-Evolving Photocatalyst $InVO_4$

Active under Visible Light Irradiation. *Chem. Phys. Lett.* **2002**, *356* (3−4), 221−226.

(7) Liu, S.; Shao, M.; Liao, F. A Novel Bio Affinity Material: The Systhesis, Biointeraction, and Electrochemical Behavior of InVO$_4$ Nanoribbons. *CrystEngComm* **2012**, *14* (10), 3441.

(8) Meng, Y.; Hong, Y.; Huang, C.; Shi, W. Fabrication of Novel Z-Scheme InVO$_4$ /CdS Heterojunctions with Efficiently Enhanced Visible Light Photocatalytic Activity. *CrystEngComm* **2017**, *19* (6), 982−993.

(9) Di Paola, A.; García-López, E.; Marcì, G.; Palmisano, L. A Survey of Photocatalytic Materials for Environmental Remediation. *J. Hazard. Mater.* **2012**, *211−212*, 3−29.

(10) Ge, L.; Xu, M.; Fang, H. Synthesis of Novel Photocatalytic InVO4-TiO2 Thin Films with Visible Light Photoactivity. *Mater. Lett.* **2007**, *61* (1), 63−66.

(11) Mondal, S.; Appalakondaiah, S.; Vaitheeswaran, G. High Pressure Structural, Electronic, and Optical Properties of Polymorphic InVO$_4$ Phases. *J. Appl. Phys.* **2016**, *119* (8), 085702.

(12) Butcher, D. P.; Gewirth, A. A. Photoelectrochemical Response of TlVO$_4$ and InVO$_4$:TlVO$_4$ Composite. *Chem. Mater.* **2010**, *22* (8), 2555−2562.

(13) Liao, L.; Zhang, Q.; Su, Z.; Zhao, Z.; Wang, Y.; Li, Y.; Lu, X.; Wei, D.; Feng, G.; Yu, Q.; Cai, X.; Zhao, J.; Ren, Z.; Fang, H.; Robles-Hernandez, F.; Baldelli, S.; Bao, J. Efficient Solar Water-Splitting Using a Nanocrystalline CoO Photocatalyst. *Nat. Nanotechnol.* **2014**, *9* (1), 69−73.

(14) Sun, S.; Wang, W.; Li, D.; Zhang, L.; Jiang, D. Solar Light Driven Pure Water Splitting on Quantum Sized BiVO$_4$ Without Any Cocatalyst. *ACS Catal.* **2014**, *4* (10), 3498−3503.

(15) Yan, M.; Yan, Y.; Wang, C.; Lu, W.; Shi, W. Ni^{2+} Doped InVO4 Nanocrystals: One-Pot Microwave-Assisted Synthesis and Enhanced Photocatalytic O2 Production Activity under Visible-Light. *Mater. Lett.* **2014**, *121*, 215−218.

(16) Vignesh, K.; Hariharan, R.; Rajarajan, M.; Suganthi, A. Visible Light Assisted Photocatalytic Activity of TiO$_2$-Metal Vanadate (M = Sr, Ag and Cd) Nanocomposites. *Mater. Sci. Semicond. Process.* **2013**, *16* (6), 1521−1530.

(17) Chaisorn, J.; Wetchakun, K.; Phanichphant, S.; Wetchakun, N. A Novel CeO$_2$/InVO$_4$ Composite with High Visible-Light Induced Photocatalytic Activity. *Mater. Lett.* **2015**, *160*, 75−80.

(18) Shen, J.; Yang, H.; Feng, Y.; Cai, Q.; Shen, Q. Synthesis of 3D Hierarchical Porous TiO$_2$/InVO$_4$ Nanocomposites with Enhanced Visible-Light Photocatalytic Properties. *Solid State Sci.* **2014**, *32*, 8−12.

(19) Lin, X.; Xu, D.; Lin, Z.; Jiang, S.; Chang, L. Construction of Heterostructured TiO$_2$/InVO$_4$/RGO Microspheres with Dual-Channels for Photo-generated Charge Separation. *RSC Adv.* **2015**, *5* (103), 84372−84380.

(20) Lin, X.; Guo, X.; Shi, W.; Guo, F.; Che, G.; Zhai, H.; Yan, Y.; Wang, Q. Ag3PO4 Quantum Dots Loaded on the Surface of Leaf-Like InVO4/BiVO4 Heterojunction with Enhanced Photocatalytic Activity. *Catal. Commun.* **2015**, *71*, 21−27.

(21) Wetchakun, N.; Wanwaen, P.; Phanichphant, S.; Wetchakun, K. Influence of Cu Doping on the Visible-Light-Induced Photocatalytic Activity of InVO$_4$. *RSC Adv.* **2017**, *7* (23), 13911−13918.

(22) Guo, F.; Shi, W.; Cai, Y.; Shao, S.; Zhang, T.; Guan, W.; Huang, H.; Liu, Y. Sheet-On-Sphere Structured Ag/AgBr@InVO$_4$ Heterojunctions and Enhanced Visible-Light Photocatalytic Activity. *RSC Adv.* **2016**, *6* (96), 93887−93893.

(23) Ji, K. M.; Deng, J. G.; Zang, H. J.; Han, J. H.; Arandiyan, H.; Dai, H. X. Fabrication and high photocatalytic performance of noble metal nanoparticles supported on 3DOM InVO$_4$-BiVO$_4$ for the visible-light-driven degradation of rhodamine B and methylene blue. *Appl. Catal., B* **2015**, *165*, 285−295.

(24) Shi, W. L.; Guo, F.; Chen, J. B.; Che, G. B.; Lin, X. Hydrothermal synthesis of InVO4/Graphitic carbon nitride heterojunctions and excellent visible-light-driven photocatalytic performance for rhodamine B. *J. Alloys Compd.* **2014**, *612*, 143−148.

(25) Habibi-Yangjeh, A.; Pournemati, K. A review on emerging homojunction photocatalysts with impressive performances for wastewater detoxification. *Crit Rev. Environ. Sci. Technol.* **2023**, *54*, 290−320.

(26) Zhang, W.; Wang, Y.; Wang, Z.; Zhong, Z.; Xu, R. Highly Efficient and Noble Metal-Free NiS/CdS Photocatalysts for H$_2$ Evolution from Lactic Acid Sacrificial Solution Under Visible Light. *Chem. Commun. (Camb)* **2010**, *46* (40), 7631−7633.

(27) Zong, X.; Yan, H.; Wu, G.; Ma, G.; Wen, F.; Wang, L.; Li, C. Enhancement of Photocatalytic H$_2$ Evolution on CdS by Loading MoS$_2$ as Cocatalyst Under Visible Light Irradiation. *J. Am. Chem. Soc.* **2008**, *130* (23), 7176−7177.

(28) Fu, J.; Chang, B.; Tian, Y.; Xi, F.; Dong, X. C3N$_4$-CdS Composite Photocatalysts with Organic-Inorganic Heterojunctions: In Situ Synthesis, Exceptional Activity, High Stability and Photocatalytic Mechanism. *J. Mater. Chem. A* **2013**, *1* (9), 3083.

(29) Yan, H.; Yang, J.; Ma, G.; Wu, G.; Zong, X.; Lei, Z.; Shi, J.; Li, C. Visible-Light-Driven Hydrogen Production with Extremely High Quantum Efficiency on Pt-PdS/CdS Photocatalyst. *J. Catal.* **2009**, *266* (2), 165−168.

(30) Peng, R.; Zhao, D.; Baltrusaitis, J.; Wu, C.-M.; Koodali, R. T. Visible Light Driven Photocatalytic Evolution of Hydrogen from Water over CdS Encapsulated MCM-48 Materials. *RSC Adv.* **2012**, *2* (13), 5754.

(31) Wang, W.; Zhu, W.; Xu, H. Monodisperse, Mesoporous Zn$_x$Cd$_{1-x}$S Nanoparticles as Stable Visible-Light-Driven Photocatalysts. *J. Phys. Chem. C* **2008**, *112* (43), 16754−16758.

(32) Li, W.; Li, D.; Chen, Z.; Huang, H.; Sun, M.; He, Y.; Fu, X. High-Efficient Degradation of Dyes by Zn$_x$ Cd$_{1-x}$ S Solid Solutions Under Visible Light Irradiation. *J. Phys. Chem. C* **2008**, *112* (38), 14943−14947.

(33) Kale, B. B.; Baeg, J.-O.; Lee, S. M.; Chang, H.; Moon, S.-J.; Lee, C. W. CdIn2S4 Nanotubes and "Marigold" Nanostructures: A Visible-Light Photocatalyst. *Adv. Funct. Mater.* **2006**, *16* (10), 1349−1354.

(34) Guo, Y.; Huang, H.; He, Y.; Tian, N.; Zhang, T.; Chu, P. K.; An, Q.; Zhang, Y. In Situ Crystallization for Fabrication of a Core-satellite Structured BiOBr-CdS Heterostructure with Excellent Visible-Light-Responsive Photoreactivity. *Nanoscale* **2015**, *7* (27), 11702−11711.

(35) Liu, X.; Fang, Z.; Zhang, X.; Zhang, W.; Wei, X.; Geng, B. Preparation and Characterization of Fe$_3$O$_4$/CdS Nanocomposites and Their Use as Recyclable Photocatalysts. *Cryst. Growth Des.* **2009**, *9* (1), 197−202.

(36) Yuan, J.; Wen, J.; Gao, Q.; Chen, S.; Li, J.; Li, X.; Fang, Y. Amorphous Co$_3$O$_4$ Modified CdS Nanorods with Enhanced Visible-Light Photocatalytic H$_2$-Production Activity. *Dalton Trans.* **2015**, *44* (4), 1680−1689.

(37) Shen, Z.; Chen, G.; Wang, Q.; Yu, Y.; Zhou, C.; Wang, Y. Sonochemistry Synthesis and Enhanced Photocatalytic H2-Production Activity of Nanocrystals Embedded in CdS/ZnS/In$_2$S$_3$ Microspheres. *Nanoscale* **2012**, *4* (6), 2010−2017.

(38) Li, G. S.; Zhang, D. Q.; Yu, J. C. A New Visible-Light Photocatalyst: CdS Quantum Dots Embedded Mesoporous TiO$_2$. *Environ. Sci. Technol.* **2009**, *43* (18), 7079−7085.

(39) Xie, Y.; Ali, G.; Yoo, S. H.; Cho, S. O. Sonication-Assisted Synthesis of CdS Quantum-Dot-Sensitized TiO$_2$ Nanotube Arrays with Enhanced Photoelectrochemical and Photocatalytic Activity. *ACS Appl. Mater. Interfaces* **2010**, *2* (10), 2910−2914.

(40) Lin, X.; Xing, J.; Wang, W.; Shan, Z.; Xu, F.; Huang, F. Photocatalytic Activities of Heterojunction Semiconductors Bi$_2$O$_3$/ BaTiO$_3$:A Strategy for the Design of Efficient Combined Photocatalysts. *J. Phys. Chem. C* **2007**, *111* (49), 18288−18293.

(41) Balachandran, S.; Swaminathan, M. Facile Fabrication of Heterostructured Bi$_2$O$_3$-ZnO Photocatalyst and Its Enhanced Photocatalytic Activity. *J. Phys. Chem. C* **2012**, *116* (50), 26306−26312.

(42) Balachandran, S.; Swaminathan, M. The Simple, Template Free Synthesis of a Bi$_2$S$_3$-ZnO Heterostructure and Its Superior Photocatalytic Activity Under UV-A Light. *Dalton Trans.* **2013**, *42* (15), 5338−5347.

(43) Balachandran, S.; Prakash, N.; Thirumalai, K.; Muruganandham, M.; Sillanpää, M.; Swaminathan, M. Facile Construction of Heterostructured BiVO$_4$-ZnO and Its Dual Application of Greater Solar Photocatalytic Activity and Self-Cleaning Property. *Ind. Eng. Chem. Res.* **2014**, *53* (20), 8346−8356.

(44) Pan, J. H.; Zhang, X.; Du, A. J.; Bai, H.; Ng, J.; Sun, D. A Hierarchically Assembled Mesoporous ZnO Hemisphere Array and Hollow Microspheres for Photocatalytic Membrane Water Filtration. *Phys. Chem. Chem. Phys.* **2012**, *14* (20), 7481−7489.

(45) Wang, Y.; Dai, H.; Deng, J.; Liu, Y.; Zhao, Z.; Li, X.; Arandiyan, H. Three-Dimensionally Ordered Macroporous InVO4: Fabrication and Excellent Visible-Light-Driven Photocatalytic Performance for Methylene Blue Degradation. *Chem. Eng. J.* **2013**, *226*, 87−94.

(46) Wu, W.; Lin, R.; Shen, L.; Liang, R.; Yuan, R.; Wu, L. Mechanistic Insight into the Photocatalytic Hydrogenation of 4-Nitroaniline over Band-Gap-Tunable CdS Photocatalysts. *Phys. Chem. Chem. Phys.* **2013**, *15* (44), 19422−19426.

(47) Fan, C.; Liu, Q.; Ma, T.; Shen, J.; Yang, Y.; Tang, H.; Wang, Y.; Yang, J. Fabrication of 3D CeVO$_4$/Graphene Aerogels with Efficient Visible-Light Photocatalytic Activity. *Ceram. Int.* **2016**, *42* (8), 10487−10492.

(48) Zhao, X.; Huang, L.; Namuangruk, S.; Hu, H.; Hu, X.; Shi, L.; Zhang, D. Morphology-Dependent Performance of Zr-CeVO$_4$/TiO$_2$ for Selective Catalytic Reduction of NO with NH$_3$. *Catal. Sci. Technol.* **2016**, *6* (14), 5543−5553.

(49) Yuan, X.; Jiang, L.; Liang, J.; Pan, Y.; Zhang, J.; Wang, H.; Leng, L.; Wu, Z.; Guan, R.; Zeng, G. In-Situ Synthesis of 3D Microsphere-Like In$_2$S$_3$/InVO$_4$ Heterojunction with Efficient Photocatalytic Activity for Tetracycline Degradation Under Visible Light Irradiation. *Chem. Eng. J.* **2019**, *356*, 371−381.

(50) Cipagauta-Díaz, S.; Estrella-González, A.; Gómez, R. Heterojunction Formation on InVO$_4$/N-TiO$_2$ with Enhanced Visible Light Photocatalytic Activity for Reduction of 4-NP. *Mater. Sci. Semicond. Process.* **2019**, *89*, 201−211.

(51) Ding, W.; Lin, X.; Ma, G.; Lu, Q. Designed Formation of InVO$_4$/CeVO$_4$ Hollow Nanobelts with Z-Scheme Charge Transfer: Synergistically Boosting Visible-Light-Driven Photocatalytic Degradation of Tetracycline. *J. Environ. Chem. Eng.* **2020**, *8* (6), 104588.

(52) Wang, X.; Chen, B.; Yan, D.; Zhao, X.; Wang, C.; Liu, E.; Zhao, N.; He, F. Distorted 1T-ReS$_2$ Nanosheets Anchored on Porous TiO$_2$ Nanofibers for Highly Enhanced Photocatalytic Hydrogen Production. *ACS Appl. Mater. Interfaces* **2019**, *11* (26), 23144−23151.

(53) Guo, F.; Shi, W.; Lin, X.; Yan, X.; Guo, Y.; Che, G. Novel BiVO$_4$/InVO$_4$ Heterojunctions: Facile Synthesis and Efficient Visible-Light Photocatalytic Performance for the Degradation of Rhodamine B. *Sep. Purif. Technol.* **2015**, *141*, 246−255.

(54) Shen, J.; Li, X.; Huang, W.; Li, N.; Ye, M. Synthesis of Novel Photocatalytic RGO-InVO$_4$ Nanocomposites with Visible Light Photoactivity. *Mater. Res. Bull.* **2013**, *48* (9), 3112−3116.

(55) Ai, Z.; Zhang, L.; Lee, S. Efficient Visible Light Photocatalytic Oxidation of NO on Aerosol Flow-Synthesized Nanocrystalline InVO$_4$ Hollow Microspheres. *J. Phys. Chem. C* **2010**, *114* (43), 18594−18600.

(56) Xiao, G.; Wang, X.; Li, D.; Fu, X. VO$_4$-Sensitized TiO$_2$ Photocatalysts for Efficient Air Purification with Visible Light. *J. Photochem. Photobiol., A* **2008**, *193* (2−3), 213−221.

(57) Hu, X.; Deng, F.; Huang, W.; Zeng, G.; Luo, X.; Dionysiou, D. D. The Band Structure Control of Visible-Light-Driven rGO/ZnS-MoS$_2$ for Excellent Photocatalytic Degradation Performance and Long-Term Stability. *Chem. Eng. J.* **2018**, *350*, 248−256.

(58) Rouquerol, J.; Avnir, D.; Fairbridge, C. W.; Everett, D. H.; Haynes, J. M.; Pernicone, N.; Ramsay, J. D. F.; Sing, K. S. W.; Unger, K. K. Recommendations for the characterization of porous solids (Technical Report). *Pure Appl. Chem.* **1994**, *66* (8), 1739−1758.

(59) Liu, B.; Liu, L.-M.; Lang, X.-F.; Wang, H.-Y.; Lou, X. W.; Aydil, E. S.; Aydil, E. S. Doping High-Surface-Area Mesoporous TiO$_2$ Microspheres with Carbonate for Visible Light Hydrogen Production. *Energy Environ. Sci.* **2014**, *7* (8), 2592.

(60) Chen, F.; Fang, P.; Liu, Z.; Gao, Y.; Liu, Y.; Dai, Y.; Luo, H.; Feng, J. Dimensionality-Dependent Photocatalytic Activity of TiO$_2$-Based Nanostructures: Nanosheets with a Superior Catalytic Property. *J. Mater. Sci.* **2013**, *48* (15), 5171−5179.

(61) Ye, L.; Liu, J.; Gong, C.; Tian, L.; Peng, T.; Zan, L. Two Different Roles of Metallic Ag on Ag/AgX/BiOX (X = Cl, Br) Visible Light Photocatalysts: Surface Plasmon Resonance and Z-Scheme Bridge. *ACS Catal.* **2012**, *2* (8), 1677−1683.

(62) Chen, L.; Huang, R.; Yin, S.-F.; Luo, S.-L.; Au, C.-T. Flower-Like Bi$_2$O$_2$CO$_3$: Facile Synthesis and Their Photocatalytic Application in Treatment of Dye-Containing Wastewater. *Chem. Eng. J.* **2012**, *193−194*, 123−130.

(63) Yuan, Q.; Chen, L.; Xiong, M.; He, J.; Luo, S.-L.; Au, C.-T.; Yin, S. Cu$_2$O/BiVO$_4$ Heterostructures: Synthesis and Application in Simultaneous Photocatalytic Oxidation of Organic Dyes and Reduction of Cr(VI) Under Visible Light. *Chem. Eng. J.* **2014**, *255*, 394−402.

(64) Lin, Y.; Li, D.; Hu, J.; Xiao, G.; Wang, J.; Li, W.; Fu, X. Highly Efficient Photocatalytic Degradation of Organic Pollutants by PANI-Modified TiO$_2$ Composite. *J. Phys. Chem. C* **2012**, *116* (9), 5764−5772.

(65) Katsumata, H.; Sakai, T.; Suzuki, T.; Kaneco, S. Highly Efficient Photocatalytic Activity of g-C$_3$N$_4$/Ag$_3$PO$_4$ Hybrid Photocatalysts Through Z-Scheme Photocatalytic Mechanism Under Visible Light. *Ind. Eng. Chem. Res.* **2014**, *53* (19), 8018−8025.

(66) Wang, D.; Kako, T.; Ye, J. Efficient Photocatalytic Decomposition of Acetaldehyde over a Solid-Solution Perovskite (Ag$_{0.75}$Sr$_{0.25}$)(Nb$_{0.75}$Ti$_{0.25}$)O$_3$ Under Visible-Light Irradiation. *J. Am. Chem. Soc.* **2008**, *130* (9), 2724−2725.